Journal of
Synchrotron Radiation

ISSN 0909-0495

Received 22 March 2010
Accepted 9 April 2010

Angle-resolved photoemission spectroscopy and imaging with a submicrometre probe at the SPECTROMICROSCOPY-3.2L beamline of Elettra

Pavel Dudin, Paolo Lacovig, Claudio Fava, Eugenio Nicolini, Anna Bianco, Giuseppe Cautero and Alexei Barinov*

Elettra-Sincrotrone Trieste ScPA, SS 14 km, 163.5 in AREA Science Park, 34149 Basovizza, Trieste, Italy. E-mail: alexey.barinov@elettra.trieste.it

The extensive upgrade of the experimental end-station of the SPECTROMICROSCOPY-3.2L beamline at Elettra synchrotron light source is reported. After the upgrade, angle-resolved photoemission spectroscopy from a submicrometre spot and scanning microscopy images monitoring the photoelectron signal inside selected acquisition angle and energy windows can be performed. As a test case, angle-resolved photoemission spectroscopy from single flakes of highly oriented pyrolitic graphite and imaging of the flakes with image contrast owing to rotation of the band dispersion of different flakes are presented.

Keywords: beamlines and optics; scanning microscopy; angle-resolved photoemission; graphite; band structure.

1. Introduction

Angle-resolved photoemission spectroscopy (ARPES) represents a unique experimental technique that offers the possibility to perform extremely accurate measurements of electronic band structure of materials. The most versatile ARPES experimental stations hosted by synchrotron radiation sources can discriminate between different types of electronic states, *i.e.* surface from bulk states or states with different symmetries (Shattke & Van Hove, 2003), owing to the capability of tuning the photon energy, polarization and, last but not least, high photon flux provided by such light sources. The modern state-of-the-art ARPES apparatus typically has energy and angle resolutions below $\sim$10 meV and $\sim$0.3°, respectively. Adding spatial resolution makes it possible to obtain much-wanted and difficult-to-obtain information on the electronic structure of an individual nano-sized object such as, for example, a graphene flake (Knox *et al.*, 2008). Recently reported photoelectron microscopes that allow ARPES measurements (Krömker *et al.*, 2008) are based on the LEEM/PEEM (low-energy electron microscopy/photoemission electron microscopy) operation principle (Bauer, 2001). They have the highest spatial resolution among all types of photoelectron microscopes; however, energy and momentum resolution in the obtained ARPES data are typically above 200 meV and 0.05 Å^{-1}, respectively.

Here we present first results of an extensive upgrade of the scanning photoelectron microscope at the SPECTROMICROSCOPY-3.2L beamline of Elettra synchrotron light source, namely the new UHV end-station, which is now hosting two exchangeable Schwarzschild objectives (SO) and an internal movable hemispherical electron energy analyzer that can perform polar and azimuthal angular scans in ultra-high vacuum (UHV) (see Fig. 1). We show that ARPES data can be acquired from a spot size of $\sim$600 nm with $\sim$33 meV total energy resolution and $\pm$0.03 Å^{-1} momentum resolution. The obtained high count rates ensure us that these limits can be reduced even further.

2. Beamline and microscope optics

The optical scheme and instrumentation up to the intermediate focus, which acts as the source for the SO, remains the same as in the original beamline set-up described by Barbo *et al.* (2000). The beamline is constructed around a variable-included-angle monochromator equipped with three spherical gratings (Melpignano *et al.*, 1994). The prefocusing and refocusing optics, each comprising a Kirkpatrick–Baez pair of mirrors, provide an overall demagnification of the undulator source (Diviacco *et al.*, 1992) by a factor of 60. At the intermediate focus the beam dimensions are typically 13 µm × 10 µm, as characterized by knife-edge test and microscopy (see Fig. 2*a*). This secondary source is demagnified further with the SO by a factor of 50, to the theoretical spot size of $\sim$200 nm in the limits of geometrical optics. The SO consists of two spherical mirrors, working at almost normal incidence, coated with multilayers optimized for high reflectivity at fixed photon energy.

Besides the implementation of spatially resolved ARPES, the upgrade aims to relieve the diffuse background present in

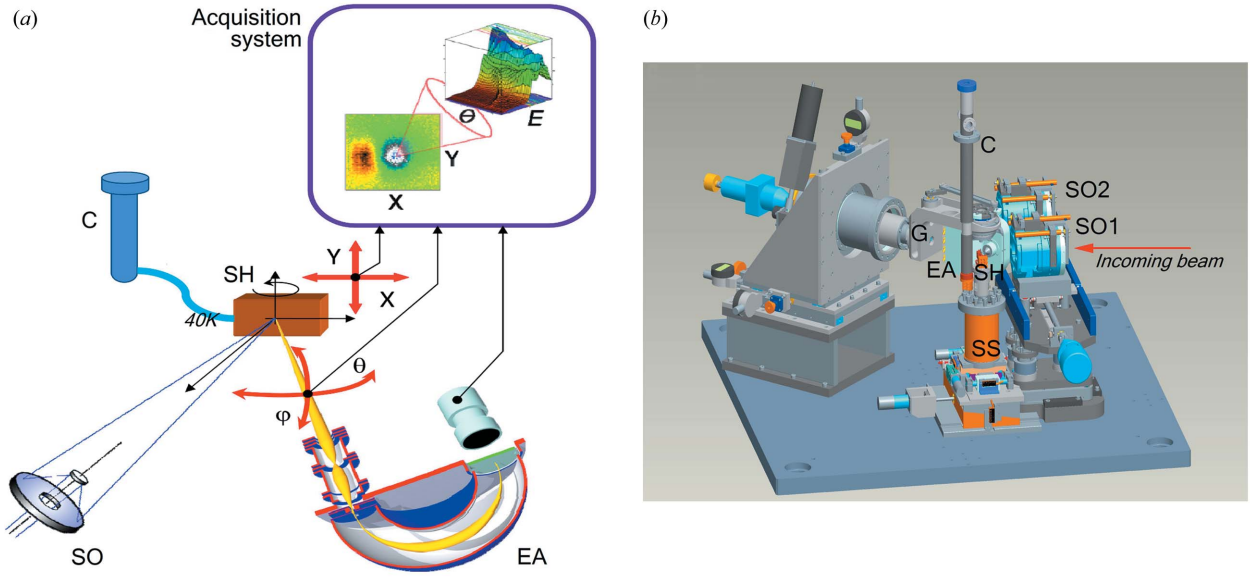

Figure 1
Principal scheme (*a*) and three-dimensional design (*b*) of the instruments inside the experimental chamber. The incoming beam is focused by one of the two Schwarzschild objectives and the sample can be scanned across the beam to obtain the photoemission intensity distribution maps within selected angle and energy windows. The main components are Schwarzschild objectives (SO1 and SO2), electron analyzer (EA), goniometer (G), sample holder (SH), scanning stage (SS) and cryostat (C).

the previous configuration with 95 eV SOs used for beam focusing since 1999 (Barbo *et al.*, 2000). The common problem for the multilayer-coated SOs, more evident at shorter wavelengths, is the coherent enhancement of non-specular reflection resulting in a few millimetres halo of scattered light around the focal point. The halo leads to the necessity of background subtraction from the photoemission spectra. To acquire a reliable spectrum from a nanostructure such as that of a nanotube (Barinov *et al.*, 2009) one has to subtract this background, which can be done only in certain sample configuration conditions and with much effort.

Keeping in mind that the intensity of the specular light is proportional to $\exp(-4\pi\sigma/\lambda)^2$, where σ is the RMS roughness of the optical surface and λ is the photon wavelength (Singh *et al.*, 1996; Bennett & Mattsson, 1989), a new SO has been coated with a multilayer optimized for photon energies as low as 27 eV. To combine both enhanced almost normal-incidence reflectivity and long-term stability up to 403 K, a Sc/Si multilayer with single Cr barrier has been deposited by d.c. magnetron sputtering at the Fraunhofer Institute for Applied Optics and Precision

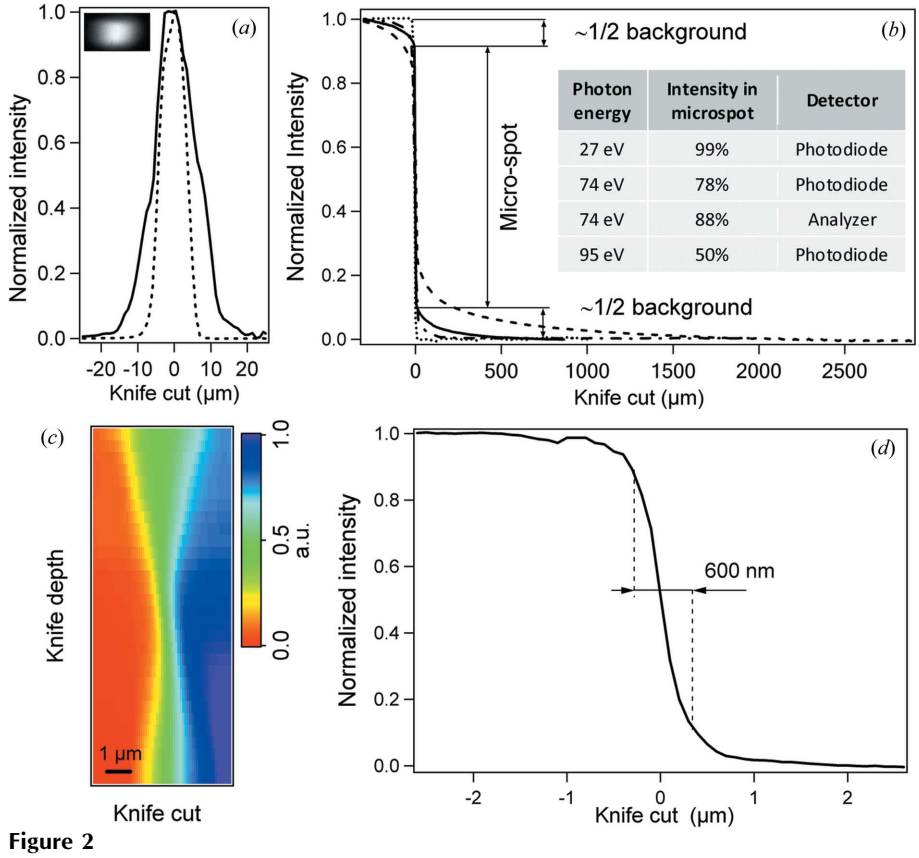

Figure 2
Microprobe characterization. Differentiated horizontal (solid) and vertical (dashed) profiles acquired with a moving blade at the intermediate focus position with a micro-image of the spot in the inset (*a*). Normalized long-distance knife-edge profiles at the SO focal plane showing the scattered background for 95 eV (dashed), 74 eV (solid) and 27 eV (dotted) SOs acquired with a photodiode (*b*). For comparison, the profile for the 74 eV SO acquired with a photoelectron analyzer is also shown (dash-and-dot). The insert table summarizes the percentage of overall intensity confined inside the focal point for different photon energies and acquisition types. Series of knife-edge profiles at the sample position varying in position along the beam axis (*c*) with the knife-edge profile in the best focus (*d*).

Table 1
Main parameters of the 27 eV multilayer.

Design	$[Si/Sc/Cr]^{10}$ + Si
Wavelength	45.5 ± 0.5 nm
Thickness Sc/period	0.4
Incidence angles	6.3–11.7°
Micro-roughness	0.8–1 nm RMS

Engineering. Table 1 summarizes the main multilayer parameters. The radii of the curvatures and the dimensions of the primary and secondary mirrors are the same as for the SOs described by Barbo *et al.* (2000).

Fig. 2(*b*) shows knife-edge profiles at the focal plane for the new 27 eV SO, as well as for 74 eV and 95 eV SOs measured with the photodiode behind the knife edge. The micro-spot is clearly distinguished as a rapid jump in the profile intensity, while slower-growing parts to the left and to the right of the jump represent the scattered background. The difference in intensity between these parts gives an estimate of their relative weight, as shown in the inset of Fig. 2(*b*). The main result is the absence of appreciable diffuse background for the 27 eV SO. The profile acquired with the electron analyzer for the 74 eV SO is also shown. The scattered background appears reduced from 22% to 12% and extends only for 150 µm, in comparison with the profile measured for the same SO with the photodiode. Such a reduction is due to the focusing properties of the electron analyzer, which selects electrons from a small area around the focal point.

The smallest spot obtained with the 27 eV SO has 600 nm FWHM (Fig. 2*d*), while the diffraction-limited beam FWHM is 230 nm (λ/NA, where NA is the numerical aperture). Such a difference is probably due to aberrations caused by figure errors of the SO mirrors. The focal depth determined for the diffraction limit (λ/NA^2) is 1.1 µm. A series of profiles acquired by changing the knife-edge position along the beam direction shows that indeed the sample must be positioned with a precision of better than 2 µm to be in focus. The flux at the sample estimated from the photodiode current measured with a SXUV photodiode (IRD) behind the 27 eV SO with 330 mA storage-ring current at 2 GeV is $\sim 8 \times 10^{10}$ photons s^{-1}, with a photon line width of <20 meV.

3. Internal movable electron analyzer

The small focal depth of the microscope reported in the previous chapter determines the high-precision requirements to the sample alignment. It is difficult to rotate the sample while maintaining the microprobe on the same spot of the surface during measurements. If both the sample and standard ARPES hemispherical analyzer with two-dimensional detector are fixed, the angular dispersion measurement would be only possible along a single azimuth. In order to obtain angular-resolved data for both polar and azimuthal angles a movable hemispherical electron analyzer with 'cross-delay line' bi-dimensional detector is introduced in a UHV. A specially designed goniometer allows the angles of data acquisition to be varied with respect to the sample surface, rotating the analyzer around two perpendicular axes with a precision of ∼0.01° and maintaining the analyzer focus fixed at the intersection of the rotation axes. The whole set-up is shown in Fig. 3(*a*). All constructive parts of the analyzer and goniometer have been designed at Elettra since no commercially available instrument could fulfil all the requirements.

The analyzer has a 40 mm mean radius with internal and external sphere radii of 20 mm and 60 mm, respectively. The distance between the sample and the analyzer entrance slit (73 mm) allows the placing of a four- to five-element electrostatic lens system. In the first version every element of the lenses, such as the internal diaphragms and slits, have been designed in order to maximize the transmission. Simion3D simulations showed that a good energy resolution, even using a relatively large analyzer entrance slit (1 mm), could be obtained at the same time as confirmed below experimentally. We present the results for a four-element lens set-up, capable of accepting emitted electrons within 1.4–8° of solid angle depending on the lens settings. Relatively high count rates [2.5–3 × 10^5 counts s^{-1} measured with a pass energy (PE) of 10 V on highly oriented pyrolitic graphite (HOPG)] encourage us to modify the lens set-up, introducing also a fifth element in order to reduce on one side the smallest acceptance angle (1.4° at the moment) and on the other side to provide for two-dimensional imaging of photoelectrons in both angle- and energy-dispersion directions.

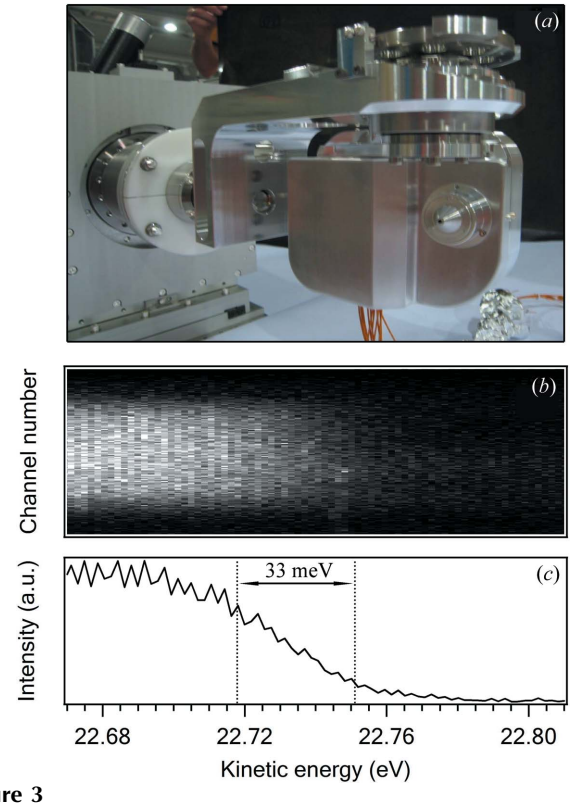

Figure 3
Internal movable electron energy analyzer mounted on the goniometer (*a*). Image of photoelectron intensity at the Fermi level of polycrystalline gold at 45 K acquired with a pass energy of 2 V on the two-dimensional detector (*b*) and its profile along the energy-dispersion direction summing all channels in the vertical (*c*).

Spectromicroscopy techniques can be considerably improved *via* multi-channel acquisition: the acquired image contains a series of spectral 'snapshots', *i.e.* for each position of the sample the photoelectron spectra (accordingly with the energy window determined by the detector size and the available PE) can be extracted from the image (Gregoratti *et al.*, 2001). For a movable internal electron analyzer the 'multi anode' requires a conspicuous number of cables, one for each channel, to be moved inside the UHV chamber in a small volume. We have chosen a two-dimensional 'cross delay line technique' because the bi-dimensional information from the detector is obtained with just four signals/cables. Moreover, this approach guarantees the highest count rate among the so-called 'centroid finding' techniques and preserves the time information for each detected electron. The working principle of this detector has already been described in detail (Siegmund, 1998; Lampton *et al.*, 1987): two cross meander delay lines, deposited on an alumina substrate, receive the pulse charge produced by the multi-channel plate (MCP) assembly (Z-stack configuration) and the impact position is determined by measuring the time interval between the electromagnetic pulse arrivals at the four extremities of the transmission line. The spatial resolution achievable with these detectors is essentially limited by the temporal resolution of the time-to-digital converter (of the order of tens of picoseconds). This allows detector designs with millions of available pixels, but in the present application MCP 'pixels' have been grouped together to 300 × 300 channels in 30 mm × 30 mm dimensions allowing energy window snapshots of up to several eV, depending on the PE (*e.g.* ∼2.5 eV for PE = 10 V).

The electronic set-up of this device is similar to the one described by Cautero *et al.* (2008). The time-resolving feature is provided by the correlation of each 'event' (acquisition of each electron) with the value of an externally triggered counter hosted by the detector electronics. The resolution is limited essentially by the counter performances. The actual detector counters are based on a FPGA (field programmable gate array) able to count up to 200 MHz, allowing a time resolution of 5 ns. The high count rates measured during the first tests allow the future employment of this feature to be foreseen, making possible spatial, temporal and angular-resolved photoemission spectroscopy experiments (STAR PES).

Summarizing this section, in the configuration used for the first tests the analyzer operates in the 'angle-integrating' or wide-angle (WA) mode with 8° acceptance angle and 'angle-resolved' or small-angle (SA) mode with an acceptance angle of 1.4°, both being single channel in the angular coordinates and multi-channel in electron kinetic energy. WA is used for fast sample scanning while the SA mode, with ± 0.03 Å^{-1} momentum resolution at the Fermi level (E_F) for 27 eV photons, is used for ARPES. The total energy resolution measured on E_F of a polycrystalline gold surface at 45 K with PE = 2 V is found to be less than 33 meV [see Figs. 3(*b*) and 3(*c*)].

4. Experimental results: HOPG test case

In order to demonstrate the capability of the instrument in the 'battle ground' we present a test case of imaging and spectroscopy of HOPG. The sample is composed of single-crystal graphite flakes of micrometre size rotated randomly around the same normal direction.

The image in Fig. 4(*a*) represents a 200 µm × 200 µm map of the integrated photoemission intensity signal in the [−0.1 to +1.9] eV binding energy window. The analyzer is set in SA mode and oriented with respect to the sample normal in a way that allows visualizing the HOPG flakes oriented with the Γ*K* direction along the acquisition azimuth. This can be done by choosing the signal of the detector channels close to E_F because only at the *K* point do the graphite energy bands approach E_F (see Fig. 5). Figs. 4(*b*) and 4(*c*) are polar angle scans acquired from the point *A* and converted in momentum space ($K\|\|$) along the corresponding Γ*K* and Γ*M* azimuths.

Even for the wide energy window of the image in Fig. 4(*a*) the contrast owing to various orientations of the flakes with

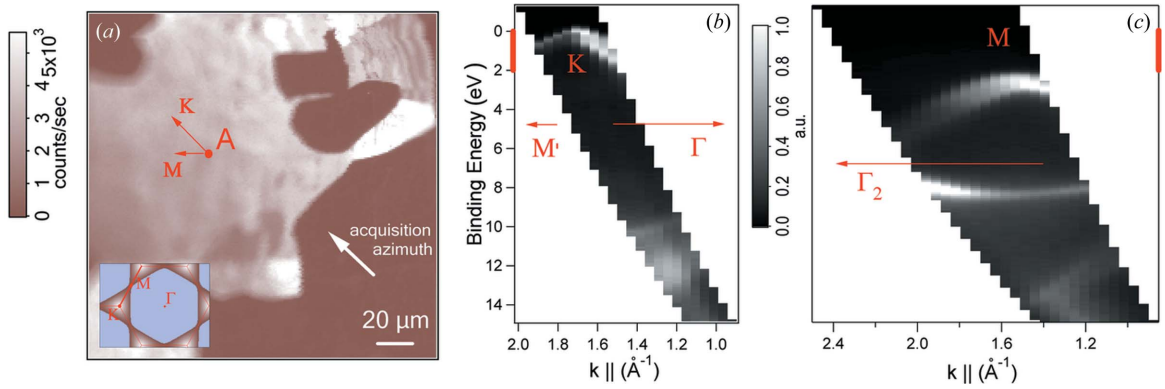

Figure 4
Spatially and angularly resolved photoelectron intensity distribution maps of HOPG. The 200 µm × 200 µm image (*a*) was acquired by the analyzer in SA mode (1.4°) in the [−0.1 to +1.9] eV binding-energy window with respect to E_F. The azimuth of the acquisition direction is shown by the thick white arrow and the polar direction was close to 41.6°, the Γ*K* radius in the first Brillouin zone (FBZ). In the inset, the colour scale of (*a*) is drawn in the FBZ of graphite showing possible variations in the orientation of the flakes with corresponding colour code along the *KMK* directions. The energy window for the image (*a*) is shown by the red line on band dispersion curves in momentum space obtained from the polar angle scans along the Γ*K* (*b*) and Γ*M* (*c*) directions from point *A* of the image.

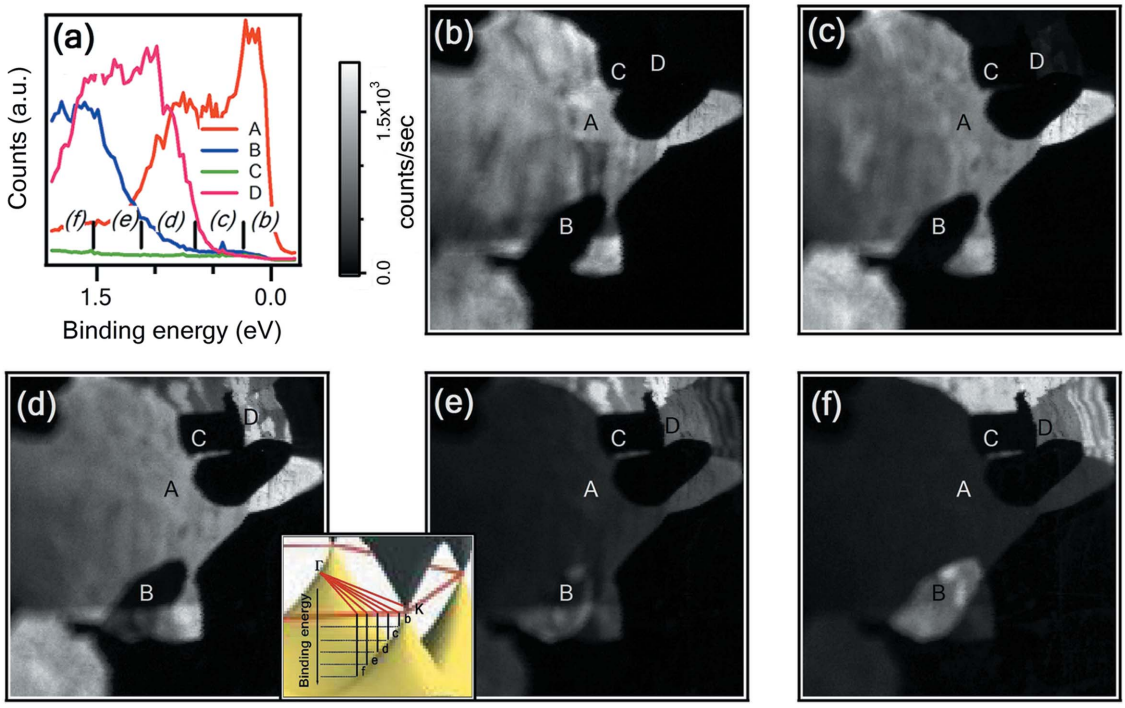

Figure 5
Spectra reconstructed from the detector channels at the points *A*, *B*, *C* and *D* (*a*). Images (*b*)–(*f*) are selected from the different parts of the detector corresponding to the electron binding energy slices indicated in (*a*). Their sum constitutes the image shown in Fig. 4(*a*). In the insert, the three-dimensional surface of the graphite band structure as a function of electron momentum is shown, with a scheme explaining the part of the band acquired by each image.

respect to the detection direction is clearly visible. The flakes oriented with the Γ*M* direction close to the acquisition azimuth give few counts (dark on the image) since their π bands do not enter into the energy window of the image, while the flakes oriented close to the Γ*K* direction give high count rates (bright). A series of images obtained from the various slices of the detector, corresponding to different binding energies, is shown in Fig. 5. The spectra reconstructed from the detector channels at the points *A*, *B*, *C*, *D* in Fig. 5(*a*) and the onset showing the three-dimensional band structure of graphite illustrate the origin of the contrast between the images: each image is tuned to have maximum counts from the flakes oriented within the appropriate angle.

The contrast between various flakes is primarily due to the rotations of their band structure with respect to each other and to a smaller extent the mosaicity of the flakes, *i.e.* the slight variation in the direction of the normal between flakes always present in HOPG (3° average deviation for the present sample) is perceived as corrugations of a large central flake in Figs. 5(*b*)–5(*d*). At the top right-hand corner of Figs. 5(*e*) and 5(*f*) near the point *D* a sequence of terraces is visible imaged as a series of bright and dark lines. If the stacking between the graphite planes of the terraces were of *AB* type typical of graphite, there would be no rotation between them and they would not be discriminated in the image. The presence of contrast indicates that the particular stack of planes represents the bulk defect in the arrangement with planes rotated one on top of the other often observed as Moiré patterns in the scanning tunnelling microscopy imaging of graphite (Osing & Shvets, 1998).

In summary, we have shown that, after extensive upgrade, the SPECTROMICROSCOPY-3.2L beamline at Elettra is capable of acquiring high-resolution ARPES spectra from a submicrometre spot with no diffuse background. The photoemission intensity distribution images in a chosen energy window and acquisition direction with respect to the sample surface can be used to study the inhomogeneity in the band structure. We believe that this instrument can be useful for shedding light on the electronic properties of strongly correlated systems, in particular those having spatial phase separation, nanostructures, small-sized crystals and inhomogeneous materials in general.

We thank Michele Bertolo and Salvatore La Rosa, who were in the beginning of SPECTROMOCROSCOPY project, Dinesh Topwal for help during the test measurements, and Fabio Barbo, Stefano Gregoratti and Luca Bella for technical support. The SO was made possible thanks to internal Elettra project VUV14 and the electron analyzer system thanks to FIRB project RBAU018KK7.

References

Barbo, F., Bertolo, M., Bianco, A., Cautero, G., Fontana, S., Johal, T. K., La Rosa, S., Margaritondo, G. & Kaznacheyev, K. (2000). *Rev. Sci. Instrum.* **71**, 5–10.

Barinov, A., Gregoratti, L., Dudin, P., La Rosa, S. & Kiskinova, M. (2009). *Adv. Mater.* **21**, 1916–1919.
Bauer, E. (2001). *J. Electron Spectrosc. Relat. Phenom.* **114**, 975–987.
Bennett, J. M. & Mattsson, L. (1989). *Introduction to Surface Roughness and Scattering.* Washington: Optical Society of America.
Cautero, G., Sergo, R., Stebel, L., Lacovig, P., Pittana, P., Predonzani, M. & Carrato, S. (2008). *Nucl. Instrum. Methods Phys. Res. A*, **595**, 447–459.
Diviacco, B., Bracco, R., Poloni, C., Walker, R. P. & Zangrando, D. (1992). *Rev. Sci. Instrum.* **63**, 388–391.
Gregoratti, L., Marsi, M., Cautero, G., Kiskinova, M., Morrison, G. R. & Potts, A. W. (2001). *Nucl. Instrum. Methods Phys. Res. A*, **467–468**, 884–888.
Knox, K. R., Wang, S., Morgante, A., Cvetko, D., Locatelli, A., Mentes, T. O., Niño, M. A., Kim, P. & Osgood, R. M. (2008). *Phys. Rev. B*, **78**, 201408.
Krömker, B., Escher, M., Funnemann, D., Hartung, D., Engelhard, H. & Kirschner, J. (2008). *Rev. Sci. Instrum.* **79**, 053702.
Lampton, M., Siegmund, O. & Raffani, R. (1987). *Rev. Sci. Instrum.* **58**, 2298–2305.
Melpignano, P., Di Fonzo, S., Bianco, A. & Jark, W. (1994). *Rev. Sci. Instrum.* **66**, 2125–2128.
Osing, J. & Shvets, I. V. (1998). *Surf. Sci.* **417**, 145–150.
Shattke, M. & Van Hove, M. (2003). Editors. *Photoelectron Spectroscopy and Related Methods.* New York: Wiley.
Siegmund, O. (1998). *Methods of Vacuum Ultraviolet Physics*, edited by J. A. Samson and D. L. Ederer. New York: Academic Press.
Singh, S., Solak, H. & Cerrina, F. (1996). *Rev. Sci. Instrum.* **67**, 1–7.